

Naval Research Laboratory

Washington, DC 20375-5320



NRL/FR/7640--09-10,174

Imaging Near-Earth Electron Densities Using Thomson Scattering

CHRISTOPH R. ENGLERT
J. MICHAEL PICONE

*Upper Atmospheric Physics Branch
Space Science Division*

DAMIEN H. CHUA
DENNIS G. SOCKER

*Solar Physics Branch
Space Science Division*

WILLIAM S. VINCENT

*Design, Test, and Processing Branch
Spacecraft Engineering Department*

JOSEPH D. HUBA
STEVEN P. SLINKER
JONATHAN F. KRALL

*Beam Physics Branch
Plasma Physics Division*

R.R. MEIER

*Department of Physics and Astronomy
George Mason University
Fairfax, VA 22030*

M. TIM CARTER

*Praxis Inc.
Alexandria, VA*

January 15, 2009

Approved for public release; distribution is unlimited

REPORT DOCUMENTATION PAGE

*Form Approved
OMB No. 0704-0188*

Public reporting burden for this collection of information is estimated to average 1 hour per response, including the time for reviewing instructions, searching existing data sources, gathering and maintaining the data needed, and completing and reviewing this collection of information. Send comments regarding this burden estimate or any other aspect of this collection of information, including suggestions for reducing this burden to Department of Defense, Washington Headquarters Services, Directorate for Information Operations and Reports (0704-0188), 1215 Jefferson Davis Highway, Suite 1204, Arlington, VA 22202-4302. Respondents should be aware that notwithstanding any other provision of law, no person shall be subject to any penalty for failing to comply with a collection of information if it does not display a currently valid OMB control number. **PLEASE DO NOT RETURN YOUR FORM TO THE ABOVE ADDRESS.**

1. REPORT DATE (DD-MM-YYYY) 15-01-2009		2. REPORT TYPE Formal Report		3. DATES COVERED (From - To) December 2007 to July 2008	
4. TITLE AND SUBTITLE Imaging Near-Earth Electron Densities Using Thomson Scattering				5a. CONTRACT NUMBER	
				5b. GRANT NUMBER	
				5c. PROGRAM ELEMENT NUMBER	
6. AUTHOR(S) Christoph R. Englert, Damien H. Chua, R.R. Meier*, Dennis G. Socker, J. Michael Picone, Joseph D. Huba, Steven P. Slinker, Jonathan F. Krall, M. Tim Carter**, and William S. Vincent				5d. PROJECT NUMBER	
				5e. TASK NUMBER	
				5f. WORK UNIT NUMBER	
7. PERFORMING ORGANIZATION NAME(S) AND ADDRESS(ES) Naval Research Laboratory 4555 Overlook Ave., SW Washington, DC 20375-5320				8. PERFORMING ORGANIZATION REPORT NUMBER NRL/FR/7640--09-10,174	
9. SPONSORING / MONITORING AGENCY NAME(S) AND ADDRESS(ES) Naval Research Laboratory 4555 Overlook Ave., SW Washington, DC 20375-5320				10. SPONSOR / MONITOR'S ACRONYM(S)	
				11. SPONSOR / MONITOR'S REPORT NUMBER(S)	
12. DISTRIBUTION / AVAILABILITY STATEMENT Approved for public release; distribution is unlimited.					
13. SUPPLEMENTARY NOTES * Department of Physics and Astronomy, George Mason University, Fairfax, VA ** Praxis Inc., Alexandria, VA					
14. ABSTRACT An innovative observational concept to image the electron density in the near-Earth environment or geospace, which includes the plasmasphere, the magnetosphere, and their boundary regions, was studied. The concept is based on the broadband detection of Thomson-scattered sunlight by the geospace electrons. This study shows that the proposed measurement is feasible with currently available technology. The major challenge of this novel type of measurement is to achieve a suitable temporal and spatial resolution while maintaining a high enough signal-to-noise ratio to separate the relatively weak Thomson scattering signal from the bright background, which is dominated by zodiacal light.					
15. SUBJECT TERMS Magnetosphere Plasmasphere Ionosphere Thomson scattering Imagine electron density					
16. SECURITY CLASSIFICATION OF:			17. LIMITATION OF ABSTRACT	18. NUMBER OF PAGES	19a. NAME OF RESPONSIBLE PERSON Christoph R. Englert
a. REPORT Unclassified	b. ABSTRACT Unclassified	c. THIS PAGE Unclassified	Unlimited	31	19b. TELEPHONE NUMBER (include area code) (202) 767-5528

CONTENTS

1.	MOTIVATION	1
1.1	Background.....	1
1.2	Expected Impacts of Geospace Imager Data	4
2.	MODELING GEOSPACE	5
2.1	Overview.....	5
2.2	Outer Magnetosphere Model: LFM	5
2.3	Ionosphere Model: SAMI3	6
2.4	Simulation Studies	7
3.	SCENE MODELING	7
3.1	Thomson Scattering Theory	7
3.2	Thomson Scattering from Near-Earth Electron Density Distributions	8
3.3	Background Sources	12
3.3.1	<i>Zodiacal Light</i>	13
3.3.2	<i>Instrumental Scattered Light</i>	16
3.3.3	<i>Hydrogen Geocorona Line Emissions</i>	18
3.3.4	<i>Solar Wind Contribution</i>	18
4.	ORBITS.....	18
5.	SIMULATED OBSERVATIONS.....	20
6.	PATH TO OPERATION.....	25
	REFERENCES	26

IMAGING NEAR-EARTH ELECTRON DENSITIES USING THOMSON SCATTERING

1. MOTIVATION

1.1 Background

The near-Earth space environment, often called “geospace,” is characterized by several regions according to their plasma properties. The taxonomy of geospace regions can be seen in Fig. 1, along with some parameters of their physical state. The lowest altitude region, called the ionosphere, is embedded in a complex neutral gas (the thermosphere) of highly varying temperature, density, and composition. The ionosphere ranges from about 90 km to approximately 1000 km. Above the ionosphere resides the plasmasphere, the interface region between the ionosphere and the magnetosphere. The plasmasphere, approximately the region of closed magnetic field lines, extends to about 2 to 6 Earth radii ($1 R_E = 6371$ km), depending on the level of geomagnetic activity (the higher the activity, the smaller the plasmasphere). The magnetosphere is an elongated region whose interface with the solar wind or bow shock is about $13 R_E$ on the sunward side of the Earth, with a “tail” that extends beyond the orbit of the Moon, at $60 R_E$. Large scale currents flow among geospace regions, which are coupled by the geomagnetic field and by electric fields generated by the flowing solar wind, the rotating ionosphere, and other processes in the thermosphere. The size and shape of the magnetosphere to first order are determined by pressure balance between the solar wind plasma and the geomagnetic field. The magnetosphere is populated with charged particles that originate in both the ionosphere and the solar wind.

The coupled geospace system is highly variable and responds rapidly to changes in solar conditions, including the solar wind and the solar extreme ultraviolet (EUV) and X-ray irradiances. As a result, “space weather” assessment and forecasting, unlike that at ground level, depends directly on knowing and forecasting conditions on the Sun. Space weather affects any operational system that uses propagation of electromagnetic waves. Electromagnetic systems include communication, navigation, position location, satellite operations, and radar. Other areas strongly impacted by space weather are astronaut safety, spacecraft charging, spacecraft operations and radiation damage, ground level power transmission, pipeline currents, telephone and aviation communications, tracking of space objects including debris, and the Global Positioning System (GPS).

The ability to assess and forecast tropospheric weather improved dramatically when new imaging devices were flown onboard satellites at the beginning of the space age. Geospace data, on the other hand, mostly come from ground and space-based in situ or transmission path sensor systems. Because the volume of geospace is some five to six orders of magnitude larger than the troposphere, the need for a global imaging capability is even greater for the understanding of space weather and to predict its impact on various operational systems.

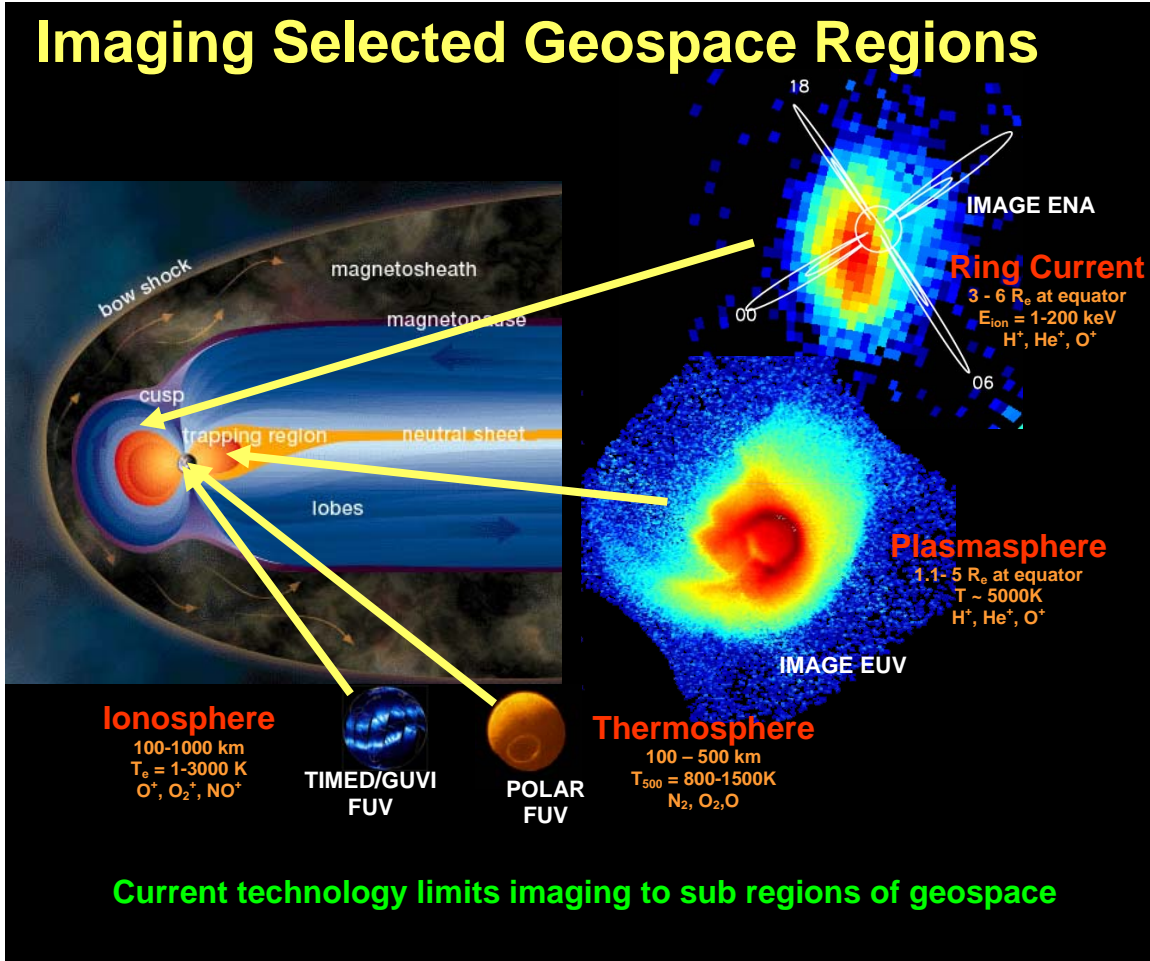


Fig. 1 – The regions of geospace and previous measurements that provide only partial coverage.
The names of the missions that obtained the images shown here are given in white.

The techniques developed so far for geospace imaging have only focused on observing proxies of the electron density, such as the helium ion emission from the plasmasphere at 30.4 nm, energetic neutral atoms (ENAs) from the ring current region of the inner magnetosphere, or far-ultraviolet imaging of the ionosphere and thermosphere. The now-decommissioned NASA Imager for Magnetopause-to-Aurora Global Exploration (IMAGE) satellite is one example of a mission that carried such imaging systems to study the response of the inner magnetosphere to changing solar wind conditions (Burch 2003, 2005). Examples of images from IMAGE and other satellites can be seen in Fig. 1. In order to derive electron densities from these images, complex models are required that relate electrons to proxy observables (to the extent that the relationship is accurately known).

While significant progress has been made by the IMAGE mission in understanding large scale processes in selected geospace regions, a major advance in the state-of-the-art would be possible if the total plasma density were to be imaged directly on a broader scale. That way, the full coupling of all geospace regions could be observed simultaneously during periods of strongly varying solar output. The interaction

with the solar wind and the propagation of plasma along with the establishment of cause and effect relationships would revolutionize space weather programs.

In fact, the solar community has been carrying out such observational programs for decades through the use of imaging devices (coronagraphs) to observe the solar corona. The technique used is “white light” imaging of the visible portion of the solar radiative flux as it undergoes Thomson scattering by electrons in the corona. The NRL LASCO imager carried onboard the NASA SOHO satellite has been obtaining such images since 1996 and is now one of the key data systems used by the Air Force Weather Agency (AFWA) and the NOAA Space Environment Laboratory (the military and civilian agencies, respectively, that have prime responsibility for space weather monitoring). The left panel of Fig. 2 shows a LASCO image of a coronal mass ejection (CME) leaving the Sun. The central panel shows the interference caused by energetic particles on the LASCO detector, 1.5 h after the CME event. The right panel demonstrates that interference of the imaging system is still being felt more than two days after the event.

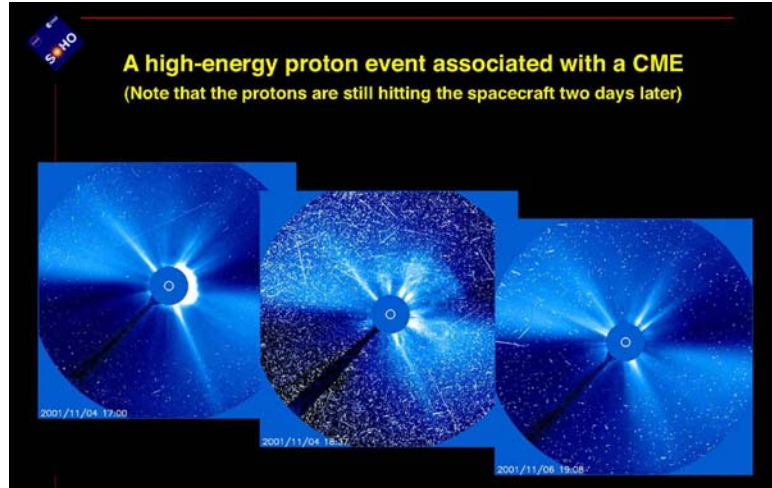


Fig. 2 – Left panel: A CME is observed. Middle panel: 97 minutes later, high energy particles interfere with the LASCO detector. Right panel: More than 50 hours after the CME event on the Sun, interference by energetic particles can still be observed. The white circles in the middle of each panel represent the size of the solar disc. The concentric monochrome discs show the size of the coronagraph occulter.

In principle, the same observational concept could be applied to geospace. This idea was first conceived in 1995 and recently published by Meier (2007a,b). While a terrestrial observing system might be similar to the solar coronagraph with an occulting disk to remove the overwhelming earthshine, the problem is rendered much more difficult by the greatly decreased solar flux at Earth and the lower geospace electron densities. Furthermore, the bright zodiacal light produces a formidable background that is superimposed on the weak geospace signal. The NRL SECCHI coronagraph on the NASA STEREO mission came tantalizingly close to making a “geocoronal” image. Figure 3 shows a composite image of the Earth and Moon taken by one of the STEREO satellites. The Sun is to the left. The much dimmer geospace emission would not be resolved in this image because the SECCHI instrument was not designed for Earth and Moon imaging. These two objects are so bright that the image is saturated (vertical saturation streaks occur).

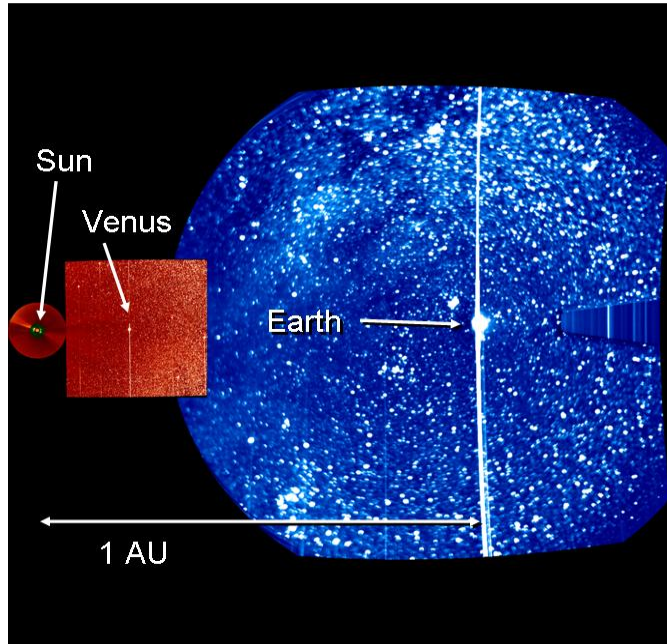


Fig. 3 – Composite image of a solar coronagraph and two heliospheric imagers on one of the STEREO satellites. In this geometry of the early mission, the Earth and the Moon, which is 0.0027AU away from the Earth, are in the field-of-view of one of the heliospheric imagers. Since the Earth and Moon are not occulted, their brightness causes a slightly tilted vertical line artifact in the image.

1.2 Expected Impacts of Geospace Imager Data

It is safe to assert that the scientific community is in agreement about the significant impact a successful geospace electron imaging mission would have. However, since no comparable measurement has ever been attempted, a mission of this kind would be a true discovery mission and, as such, its impact is impossible to predict or quantify in its entirety. Yet, there is a clear sense that the measurement of the temporal evolution of the electron distribution in the geospace environment will facilitate a true leap forward in our understanding of the physical processes involved and, thus, in our ability to develop and verify forecasting capabilities that will find wide usage in the military and civilian communities. The availability of geospace electron density distribution data will facilitate the development of new generation, physics-based assimilation models that have a high potential of significantly improving the currently available forecasting capabilities.

In summary, a geospace imaging mission will:

- Determine how electrons in the magnetosphere, plasmasphere, and ionosphere are redistributed in response to solar wind forcing.
- Understand mechanisms of solar wind plasma entry into the magnetosphere by globally imaging structures along the magnetopause and magnetospheric boundary layers.
- Determine how variations of the dusk side plasmasphere and plasmapause are coupled to the global dynamics of the magnetosphere.

- Establish sensitivity of space weather forecasts to initial conditions in the magnetosphere and provide global boundary conditions to geospace specification models.

Applications and operational fields that are likely impacted by such a leap in our understanding of geospace include the improvement of space situational awareness and anomaly resolution, the forecasting of satellite environments, assessment of communication capabilities, and potentially Global Positioning System (GPS) accuracies and outages.

In this work, we have carried out a study that demonstrates the feasibility of imaging geospace electrons using the Thomson scattering technique. Section 2 discusses the models we employed to determine time sequences of geospace plasma distributions used for this study. Section 3 explains how we use these plasma distributions to calculate the signal brightness from the Thomson scattering and several important background sources. In Section 4, we examine the suitability of various orbits for imaging the near-Earth space environment using Thomson scattering. Scene simulations are shown in Section 5. These simulated images include estimated instrument properties, measurement noise, and realistic signal and background brightnesses. Section 6 briefly outlines the path to a potential future operational capability using this proposed measurement concept.

2. MODELING GEOSPACE

2.1 Overview

The near-Earth space environment (geospace) comprises the solar wind, outer and inner magnetosphere, plasmasphere, ionosphere, and thermosphere. The primary driver of geo-effective events that can disrupt space-based systems (e.g., communication, navigation) are solar eruptions such as coronal mass ejections and solar flares. These disturbances propagate through interplanetary space in the solar wind and impinge upon the Earth's magnetic field thereby affecting the entire near-earth space environment. A major thrust today in space physics research is to self-consistently model this environment based on first-principles physics. The goal is to acquire the capability to predict and assess the impact of major solar events on military and civilian space-based systems.

The initial thrust in model development was to treat each component of the near-earth space environment separately and invoke relatively simple boundary conditions to account for neighboring regions. A primary reason for this initial approach, other than limited computational resources, is that different physical models are suited to each region. For example, to lowest order, a single-fluid magnetohydrodynamic (MHD) model is appropriate to model the magnetosphere while a multi-ion, electrostatic model is appropriate for the ionosphere. However, with the advent of improved and relatively inexpensive computer systems (e.g., Beowulf clusters), considerable effort is underway to develop a self-consistent model of geospace by coupling individual physics based models.

2.2 Outer Magnetosphere Model: LFM

The Lyon-Fedder-Mobarry (LFM) model is a 3-D, MHD simulation of the response of the Earth's magnetosphere to the solar wind and the interplanetary magnetic field (IMF). The model solves the MHD equations for the Earth's magnetosphere. A summary of the numerical algorithms can be found in (Fedder and Lyon 1995; Mobarry et al. 1996; Lyon et al. 2004). LFM solves a potential equation $\nabla \cdot \Sigma \nabla \Phi = F(J_{\parallel})$, where J_{\parallel} is the current parallel to the field line, which is mapped in from the magnetosphere. The conductance tensor Σ has two parts: a solar EUV conductance and an auroral precipitation-enhanced conduc-

tance. The solar contribution depends on the observed solar radio flux at 10.7 cm and the zenith angle. In the model the seasonal and diurnal variations of the magnetic dipole are taken into account. The solar contribution to the Pedersen and Hall conductances come from a fit to incoherent scatter radar data. The auroral contribution to the ionospheric conductance involves estimating a precipitating electron energy flux, including effects due to field-aligned potential drops, and then using the data fits of Robinson et al. (1987), to estimate the conductances. Recently, this semi-empirical model of the ionospheric conductivities has been replaced with conductivities derived from SAMI3 (see Section 2.3).

The LFM model has been under development for more than a decade and has been subjected to many tests of its numerics. It has been used to study magnetospheric questions in model problems (Fedder et al. 1995a), that is, problems in which an ideal or steady condition of the system is used. Currently, work with the simulation model is concentrated on actual events, where the input to the simulation is measured solar wind data, and the output is compared to measured data (Fedder et al. 1995b; Fedder et al. 1997; Slinker et al. 1998, 1999a). Additionally, excellent agreement between the simulation results, the Advancement and Validation of Real-Time Assimilative Mapping of Ionospheric Electrodynamics (AMIE) analysis, and Defense Meteorological Satellites Program (DMSP) measurements for substorm conditions (Slinker et al. 1999b) have been obtained.

2.3 Ionosphere Model: SAMI3

SAMI3 is a three-dimensional, physics-based model of the ionosphere. It is based on SAMI2 (Huba et al. 2000), a two-dimensional model of the ionosphere. SAMI3 models the plasma and chemical evolution of seven ion species (H^+ , He^+ , N^+ , O^+ , N_2^+ , NO_2^+ and O_2^+). To our knowledge SAMI3 is the only ionosphere code that models full plasma transport for all ion species, including the molecular ions. The complete ion temperature equation is solved for three ion species (H^+ , He^+ , and O^+) and the electron temperature equation is solved. In the current version of SAMI3, the neutral composition and temperature are specified using the empirical Naval Research Laboratory Mass Spectrometer - Incoherent Scatter Radar (NRLMSISE00) model (Picone et al. 2002) that is based on MSIS86 (Hedin et al. 1991), and the neutral wind is specified using the Horizontal Wind Model (HWM) (Hedin 1987). We note that SAMI3 is being coupled to a Thermosphere Ionosphere Mesosphere Electrodynamical General Circulation Model (TIMEGCM) under a NASA program; it is anticipated that this coupled model will be available in CY2010.

SAMI3 uses a flexible dipole model of the Earth's geomagnetic field; in the low- to mid-latitude ionosphere, it mimics the International Geomagnetic Reference Field (IGRF) by fitting a dipole field to IGRF at each longitude in the grid while at high latitude it uses a standard dipole model (tilted or untilted). The latitudinal extent of SAMI3 is $\pm 89^\circ$ and the altitude range is up to $\approx 8 R_E$. SAMI3 has been self-consistently coupled electrodynamically to - the LFM magnetosphere model and to the Rice Convection Model (RCM) (Huba et al. 2005). SAMI3 uses a non orthogonal, non-uniform, fixed grid. The grid is closed: there are no open field lines in the high latitude ionosphere that require specified boundary conditions. Moreover, the grid is designed to optimize the numerical mesh so that the spatial resolution decreases with increasing altitude. The plasma is transported transverse to the geomagnetic field using a finite volume method in conjunction with the donor cell method. The code is fully parallelized using the Message Passing Interface (MPI) method, which is critical to computational efficiency for large-scale simulations.

2.4 Simulation Studies

Two simulation studies of geomagnetic storms were performed using the coupled SAMI3/LFM codes: the January 14, 1988 and August 24, 2005 storms. The purpose of these runs was to provide realistic data sets for the design of a geocoronagraph imager. The primary output from the modeled results was the total electron content as a function of time as viewed from the L1 Earth/Sun Lagrange point and from a position $30 R_E$ above the North Pole. These data sets were converted to brightnesses based upon Thomson scattering theory and used to determine the constraints on a geocoronagraph to observe the electron density in the near-Earth space environment.

3. SCENE MODELING

A primary task in determining the feasibility of measuring the Thomson scattered light from geospace electrons is simulating the scene to be observed. All sources of light that fall within the expected observation passband must be taken into account. These include the Thomson scattering from geospace electrons that we wish to observe in addition to a number of background sources against which our target signal will be measured. In Sections 3.1 and 3.2, we describe the theory and model outputs used in computing the Thomson scattering brightness from geospace electrons. Section 3.3 summarizes the background sources that are expected in the observed scene and how their intensities are computed.

3.1 Thomson Scattering Theory

The solar radiance (photons $\text{cm}^{-2} \text{s}^{-1} \text{sr}^{-1}$) scattered by geospace electrons seen by an observer at location \mathbf{r} , viewing in direction \mathbf{n} can be written as

$$I(r, \hat{n}) = \int \varepsilon(r', \hat{n}) e^{-\tau(r, r')} ds(r') \quad (1)$$

where ε is the volume scattering rate of photons ($\text{cm}^{-3} \text{s}^{-1} \text{sr}^{-1}$) at location \mathbf{r}' in direction \mathbf{n} toward r , and τ is the extinction optical depth. For Thomson scattering of visible radiation, the optical depth is assumed to be zero (except for viewing from the ground, albeit airglow may prevent observing from that location). The integration is carried out along the path $d\mathbf{s}$ between \mathbf{r}' and \mathbf{r} . This formal description of the radiance does not incorporate polarization, but does account for anisotropic scattering (see below), which is closely related to polarization. See Vourlidas and Howard (2006) and their references for more details.

The volume scattering rate is given as:

$$\begin{aligned} \varepsilon(r', n) &= N_e(r') \sigma \varphi(\theta) \int F(R_h, \lambda) d\lambda \\ &= N_e(r') g \varphi(\theta) \end{aligned} \quad (2)$$

where N_e is the electron number density (cm^{-3}) and the g -factor is the rate of scattering of solar white-light photons (number of scatterings per second per electron) given by the product of the (wavelength-independent) Thomson scattering cross section, σ (cm^2), and the solar flux at Earth, F , integrated over the wavelength (λ) band of interest (in units of photon $\text{cm}^{-2} \text{s}^{-1}$). The scattering phase function is $\varphi(\theta) = 3/(16\pi)(1 + \cos^2 \theta) \text{ sr}^{-1}$, where θ is the scattering angle. Note that the solar flux variation with the inverse square of the heliospheric distance, R_h , can safely be ignored for geospace, but is important for evaluating the background contribution from solar wind electrons.

Substituting the volume scattering rate from Eq. (2) into Eq. (1) and assuming an optically thin regime yields:

$$I(r, \hat{n}) = g\varphi(\theta)\int N_e(r')ds(r') \quad (3)$$

The intensity may be converted to column emission rate in Rayleighs (R) upon multiplication by $4\pi/10^6$. If the scattering angle θ does not change along the line of sight, the integral on the RHS of Eq. (3) becomes $\int N_e ds$, which is the total electron content (TEC) or the column density of electrons (number of electrons in a 1 cm^2 column along the line-of-sight).

Values for the quantities in Eqs. (1-3) are as follows. The Thomson cross section is $\sigma = 6.66 \times 10^{-25}\text{ cm}^2$. The integrated solar flux between 490 and 870 nm is $F = 1.42 \times 10^{17}\text{ photon cm}^{-2}\text{ s}^{-1}$, based on data from the Solar Irradiance Monitor (SIM) instrument on the Solar Radiation and Climate Experiment (SORCE) satellite on 25 Jan 2003 (Harder et al. 2005). This wavelength band avoids the geocoronal hydrogen Balmer- β line at 486.1 nm and higher order Balmer lines, whose emissions can extend to several tens of R_E altitude. (Balmer- α at 656.3 nm is a special case, discussed below). Thus, the g-factor is $g = \sigma F = 9.88 \times 10^{-8}\text{ s}^{-1}$. As the solar radiation in this wavelength band varies little over a solar cycle (< 0.1%), g is effectively constant.

Earthshine produces a secondary source of illumination which increases the Thomson scattering signal. While we have not explicitly incorporated it in the formalism, its inclusion is straightforward (e.g., Qiu et al. (2003)).

Initial estimates of typical signal levels indicate the feasibility of the Thomson scattering measurement approach. In the ionosphere, for an observer viewing the entire vertical column of electrons, the typical total electron content at solar minimum is 10 TEC units (1 TEC unit = $10^{12}\text{ electron cm}^{-2}$). For viewing vertically outward from 100 km in a direction 90° from the Sun, the column emission rate is about 1.4 R. At solar maximum, the value might be 4-5 times larger due to the increased ionization by solar EUV radiation. These levels can be detected with current technology. For the plasmasphere, we derive a simple scaling of existing helium 30.4 nm images to obtain an estimate of the Thomson scattering signal. Typical 30.4 nm column emission rates observed from the IMAGE satellite are of order 1-20 R (taken from calibrated images supplied by B. Sandel, private communication, 2007). This is crudely scaled to a Thomson scattering column emission rate upon multiplication by the ratio of the g-factor, above, to that for helium ($1.8 \times 10^{-5}\text{ s}^{-1}$ at solar minimum; see Meier (1991; p. 52), after correction for a factor of 2 error in a referenced solar 30.4 nm line profile), and the ratio of the electron column content to that of He^+ (approximately a factor of 10, but see below). Ignoring differences in phase functionality, the scaling of 30.4 nm to Thomson scattering is about a factor of 5.5×10^3 . Thus, the plasmaspheric column emission rate for Thomson scattering is 0.1 to 2 R, again a measurable quantity with current technology. A caveat in this scaling of He^+ images is that significant variability can occur in the relative abundance of helium ions to the total plasma (Craven et al. 1997; Krall et al. 2008). It is, indeed, this variability that motivates direct measurements of the actual electron density, to mitigate reliance on proxies.

3.2 Thomson Scattering from Near-Earth Electron Density Distributions

Using the output of the SAMI3 and LFM models and the formalism described in Section 3.1, we compute the brightness of Thomson scattered sunlight from geospace electrons. At radial distances between $1.02 R_E$ and $4.5 R_E$ three-dimensional electron densities are specified by SAMI3. For radial distances greater than $4.5 R_E$, electron densities are given by LFM. The line-of-sight electron column densi-

ties (TEC) required in Eq. (3) are computed from these model outputs and are placed on a common grid in geocentric solar magnetospheric (GSM) coordinates¹. TECs were initially computed from a viewing location at the Sun-Earth L1 Lagrange point² for both quiet solar wind conditions and during a geomagnetic storm period on August 24, 2005 (Fig. 4).

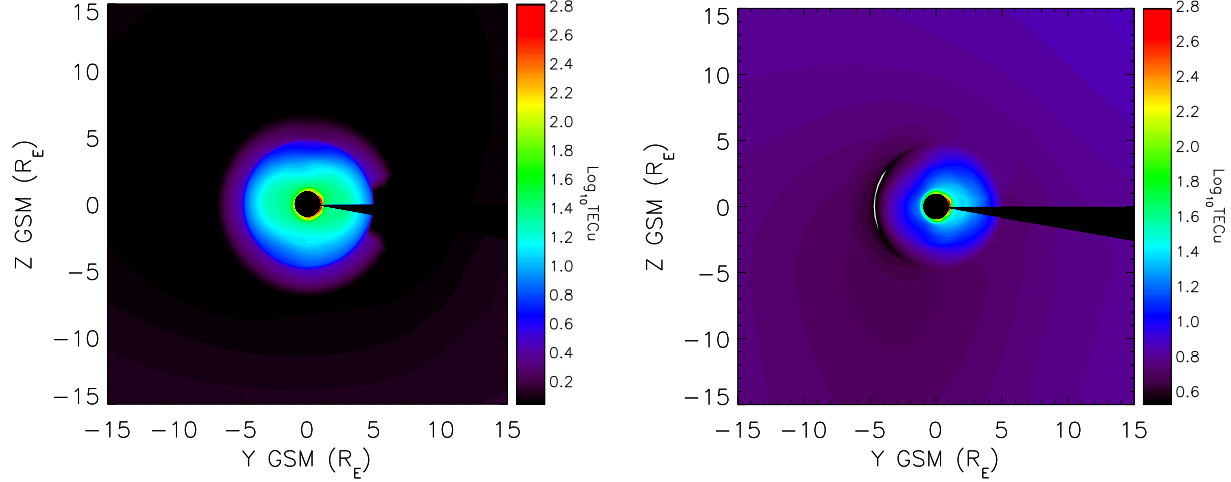


Fig. 4 – Line-of-sight column electron densities (TEC) from a viewing location at the Sun-Earth L1 Lagrange point for quiet (left) and storm-time (right) conditions.

For both the quiet-time case on January 1, 2007, and the storm-time scenario on August 24, 2005, the solar flux between 490-870 nm was about 1.42×10^{17} photons $\text{cm}^{-2} \text{ s}^{-1}$, giving a g -factor of $9.44 \times 10^{-8} \text{ s}^{-1}$. Multiplication of the TECs shown in Fig. 4 by the g -factor and the phase function for a scattering angle of 180° yields the Thomson scattering brightness as shown in Fig. 5. These images are shown on a log scale between 0.01 and 100 Rayleighs. The Earth is at the center and is blocked by a modeled occulting disk with a radius of $1.08 R_E$.

The Thomson scattering signal for quiet solar wind conditions (Fig. 5, left panel) is between 0.1-0.5 Rayleighs in most regions of the magnetosphere. Within the modeled plasmasphere (shown here by the circular region inside of 5 RE) the Thomson scattering signal increases with decreasing radial distance as electron densities grow larger closer to the Earth. Within the quiet-time plasmasphere the Thomson scattering brightness is about 5 Rayleighs and increases to a few tens of Rayleighs in the topside ionosphere at the edge of the inner field of view.

¹ In the GSM coordinate system, the x-axis extends from the Earth to the Sun and the positive z-axis is the projection of the northern magnetic pole in the plane perpendicular to the x-axis.

² The Sun-Earth L1 Lagrange point is the location at which the gravitational forces exerted on an object from the Sun and the Earth balance. It is located about $1.5 \times 10^6 \text{ km}$ from Earth.

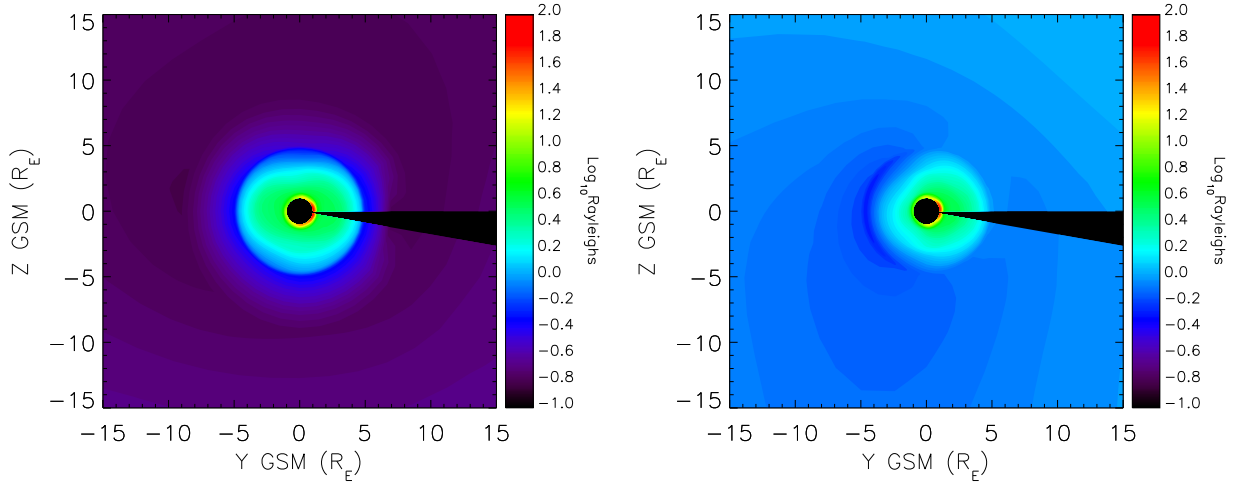


Fig. 5 – Thomson scattering signal from geospace electrons as seen from L1. The left panel corresponds to a quiet-time period while the right panel is for a storm-time scenario.

For the August 24, 2005, magnetic storm scenario shown in Fig. 5 (right panel), the electron densities throughout the magnetosphere are elevated in comparison to the quiet-time case. The Thomson scattering brightness has proportionally increased here, with intensities around 1 Rayleigh in the magnetosphere. Although the Thomson scattering brightness in the storm-time plasmasphere is comparable to the quiet-time case, we see that the plasmasphere has reduced in size and is asymmetric, with more electron density concentrated on the dusk-side of the Earth. This is consistent with observations during storm periods when enhanced convection in the magnetosphere erodes away the plasmasphere (Goldstein et al. 2003). Note that for the viewing geometry from L1, most of the signal seen originates in the dawn-dusk plane which limits the ability to infer longitudinal structures.

We also evaluated Thomson scattering from electron densities in the near-Earth space environment from a viewing location above the North Pole of the Earth, looking down from a satellite in a circular or elliptical polar orbit at an altitude of 30 RE. This high altitude is necessary to capture the equatorial cross-section of the Earth’s magnetosphere in one scene.

For this polar viewing scenario, line-of-sight electron column densities were computed from the LFM and SAMI3 models at 7.5 minute time steps during a 15 hour period for the simulation of the August 24, 2005 storm event. Computation of the Thomson scattering brightness for polar viewing is the same as that for the L1 case except that a scattering angle of 90° is used in computing the phase function. This reduces the Thomson scattering signal by a factor of two. Despite this reduction in signal, there are several advantages to the polar viewing location over looking from L1, which we will demonstrate in the following.

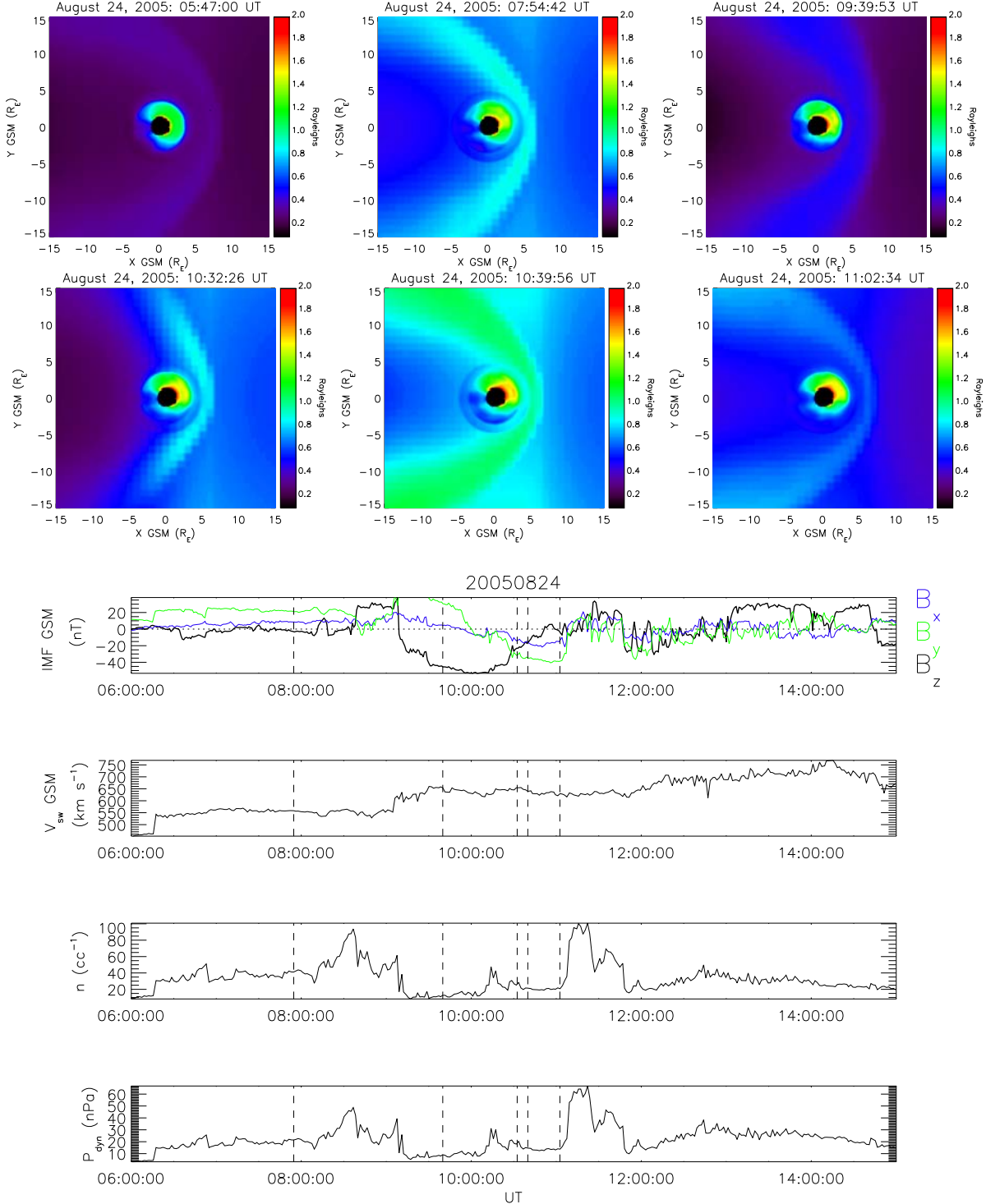


Fig. 6 – Thomson scattering signal from geospace electrons as seen from a polar viewing location at various times during the August 24, 2005, geomagnetic storm event. The bottom panel shows the corresponding solar wind data (from top to bottom – magnetic field, magnetic field clock angle, velocity, density, and dynamic pressure). The dashed lines in the bottom panels indicate the times that correspond to the Thomson scattering signal images shown above.

The simulated Thomson scattering signals as viewed from a polar perspective reveal important magnetospheric features in the scene that are not present when looking at geospace from L1. These include the bow shock, magnetosheath, and magnetopause. The Earth's bow shock is a shock wave that forms when the solar wind flowing at supersonic velocities encounters the magnetosphere and is deflected. In Fig. 6, the solar wind flows from right to left and the bow shock is the flared boundary 5–10 R_E upstream from the Earth. The magnetosheath is the region Earthward of the bow shock but still outside the magnetosphere and consists of shocked solar wind particles. In Fig. 6, the magnetosheath is the region of varying thickness just beyond the bow shock. At the inner boundary of the magnetosheath is the magnetopause, which is the outer-most boundary of the magnetosphere, inside which the Earth's magnetic field dominates the dynamics.

The location of the bow shock and magnetopause and the thickness of the magnetosheath vary with the solar wind. Leading up to a geomagnetic storm, significant increases in the solar wind velocity, density, and magnetic field are generally observed, especially during coronal mass ejection events. In response the bow shock and magnetopause are pushed Earthward as shown in the middle panels of Fig. 6. This contraction is especially important during strong storm events when the magnetopause is pushed inside of geosynchronous orbit ($R = 6.6 R_E$), exposing satellites in that orbit to the solar wind. Observation of these conditions by an instrument measuring the Thomson scattering signal will be able to warn satellite operators of such conditions in addition to providing invaluable data for spacecraft anomaly resolution.

The local time and longitudinal variation of plasmaspheric features can be characterized and studied by examining the Thomson scattering signal from a polar perspective. For example, the duskside drainage plume observed by the IMAGE EUV instrument (Fig. 1) (Goldstein et al. 2003) will be visible from this polar vantage point. Plasmaspheric drainage plumes are regions of cold, dense plasma that are transported outward from the plasmasphere into the outer magnetosphere by enhanced convection during geomagnetic storms. By mapping these features down geomagnetic field lines, Foster et al. (2002) have shown that these drainage plumes correspond to regions of greatly enhanced TEC in the ionosphere that are associated with regions that experience the most pronounced disruptions in communications and navigation capabilities during storms. Observations of this drainage plume feature will be critical in furthering our understanding of the coupling between the plasmasphere and magnetosphere. Although the plasmasphere is visible in the Thomson scattering scene as viewed from L1 we only view the dawn and dusk plane of this region of geospace from that perspective. Other longitudinal variations would only appear as changes in the scene brightness when looking from L1.

Measurement of the Thomson scattering signal from geospace electrons will be an extremely useful tool in capturing both the spatial and temporal variation of the magnetosphere, plasmasphere, and ionosphere in response to solar wind forcing.

3.3 Background Sources

When viewing the near-Earth space environment in the visible part of the spectrum, a number of background sources contribute to the scene. Sources such as zodiacal light, emissions from terrestrial emission lines, and scattered light from the solar wind are significantly more intense than the target Thomson scattering signal. In this section, we discuss the primary sources of background light in the scene and our calculations to estimate their brightness.

3.3.1 Zodiacal Light

The zodiacal light is solar radiation scattered from dust particles in the heliosphere. Its brightness is a function of viewing direction, distance from the Sun, wavelength, and the position of the observer relative to the ecliptic plane. We estimate the zodiacal light brightness using the results compiled by Leinert et al. (1998). Figure 7 shows the zodiacal light brightness distribution in units of Rayleighs per Ångstrom as a function of ecliptic latitude and longitude at a wavelength of 500 nm. At low ecliptic latitudes, one is looking in or near the ecliptic plane, while at high ecliptic latitudes, one is looking perpendicular to it. At 0° ecliptic longitude, one is looking at the Sun, 90° ecliptic longitude is perpendicular to the Sun-Earth line, and 180° ecliptic longitude is in the anti-Sunward direction. It is assumed that the zodiacal light brightness is symmetric about the ecliptic plane and that it is azimuthally symmetric about the origin at the Sun.

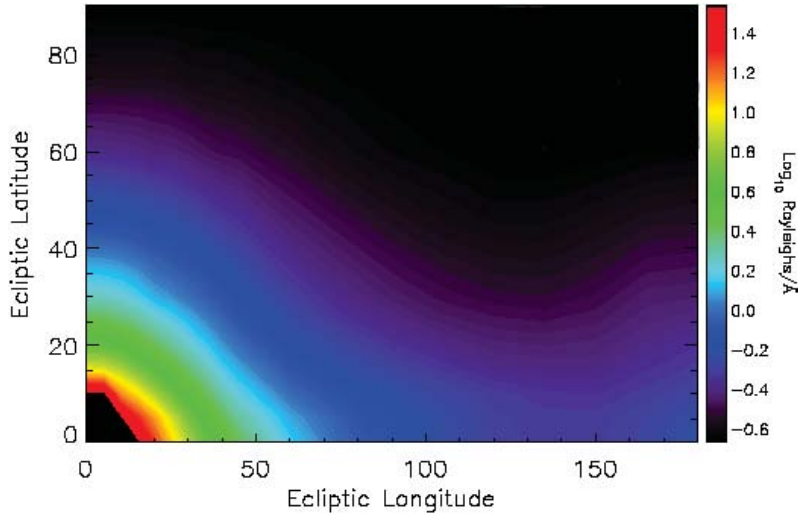


Fig. 7 – Zodiacal light brightness as a function of ecliptic latitude and longitude. The brightness is given in units of Rayleighs per Angstrom. From Leinert et al. (1998).

For a viewing location at L1 with a field of view subtending 7° , the lines of sight will remain largely in the ecliptic plane looking in the anti-sunward direction toward an ecliptic longitude of 180° . The modeled zodiacal light background brightness for the L1 viewing location is shown in Fig. 8. The viewing geometry is the same as that for Fig. 5. The zodiacal light is shown to be slightly enhanced around the direct anti-Sunward direction with brightnesses around 2770 Rayleighs. This is the *gegenschein* phenomenon, in which the brightness of the sunlight reflected by interplanetary dust particles is enhanced near the direct anti-Sunward direction due to backscattering.

The zodiacal light dominates the scene as the most significant background source. Its brightness is two to three orders of magnitude larger than our target Thomson scattering signal from geospace electrons when viewing the near-Earth space environment from L1. In contrast, when looking down at the Earth's magnetosphere, plasmasphere, and ionosphere from a polar perspective, the zodiacal light background is reduced significantly. For this polar viewing location, we treat the zodiacal light as a uniform background with a brightness of 0.24 Rayleighs per Ångstrom (Fig. 7). Across our band pass of 490 to 870 nm, this

brightness amounts to 929 Rayleighs. The zodiacal light background is reduced by about a factor of three when viewing geospace from a polar perspective in comparison to viewing the Earth from L1. This is because the interplanetary dust is largely confined to the ecliptic plane and when looking down through it, as from a polar viewing location, the path length is much shorter than when looking along the ecliptic (as from L1).

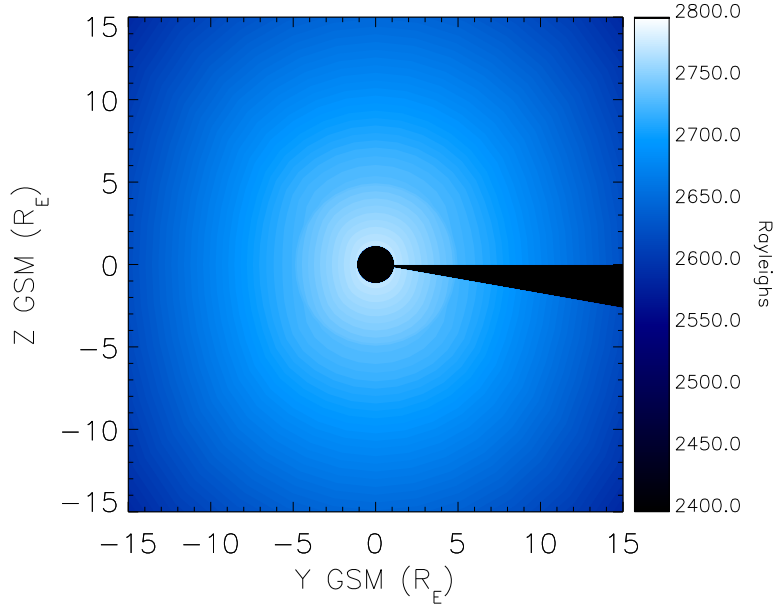


Fig. 8 – Zodiacal light scene brightness for a viewing location at L1 looking back at the Earth. The modeled brightness distribution derives from data compiled by Leinert et al. (1998).

To corroborate the zodiacal light brightness estimates of Leinert et al. (1998) that are used in these calculations, we examined a number of other published sources. The high-resolution zodiacal light brightness distribution published by Kwon et al. (2004) is consistent with that of Leinert et al. (1998) to within 12% within the *gegenschein* region and within 6% when looking up toward the ecliptic pole. We also examined the output from the Koutchmy-Lamy model of the solar F-corona (Koutchmy and Lamy 1985), which is another designation of the zodiacal light used in solar physics. Figure 9 shows the brightness of the F-corona as a function of radial distance from the Sun in units of solar radii from the Koutchmy-Lamy model. The zodiacal light brightness in the ecliptic plane (solid line) and looking out toward the poles of the ecliptic (dashed line) are shown in the top panel. The bottom panel shows the ratio of the equatorial to polar zodiacal light brightness. At 1 AU ($215 R_{\text{Sun}}$), the ratio of equatorial to polar zodiacal light brightness is about 3.3, which is consistent with the Leinert et al. (1998) value that we used in our calculations.

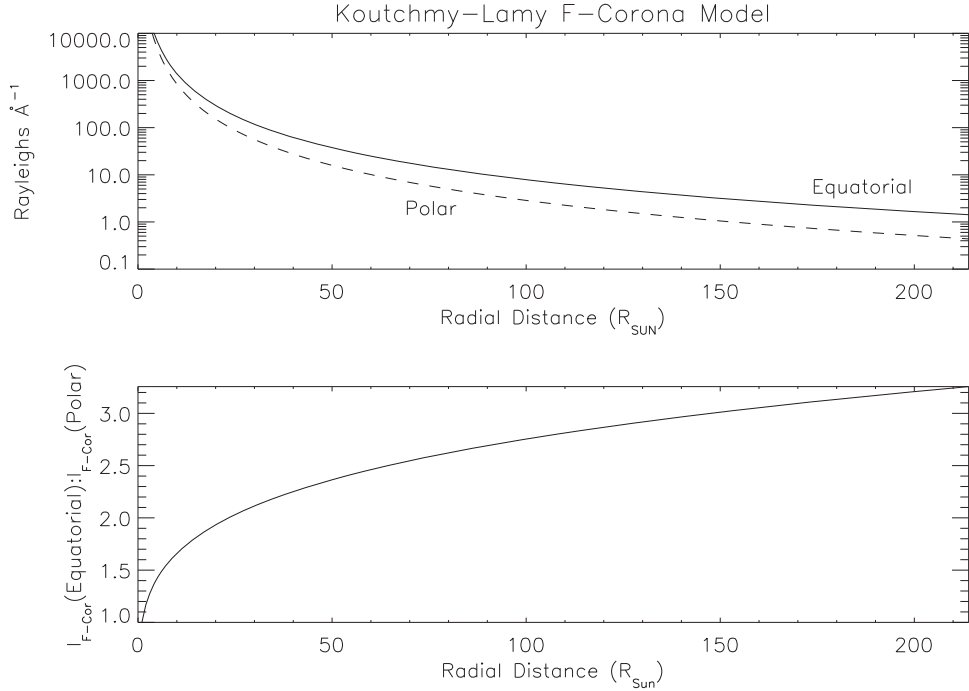


Fig. 9 – Koutchmy-Lamy model of the solar F-corona, or zodiacal light, derived from SOHO LASCO measurements. The F-corona brightness within the plane of the ecliptic is shown in the top panel by the solid trace while the brightness when looking perpendicular to the ecliptic plane at high ecliptic latitudes is given by the dashed line. The bottom panel shows the ratio of the equatorial to polar brightness of the zodiacal light.

The Thomson scattering measurement will be dominated by the zodiacal light for both the L1 and polar viewing locations although its contribution to the total scene brightness is reduced by about a factor three for the latter case. However, some key properties of the zodiacal light will make it tractable to subtract this background from the observed scene. The zodiacal light is smoothly distributed and symmetric with respect to the ecliptic plane and helioecliptic meridian. Moreover, the zodiacal light brightness in the visible part of the solar spectrum is largely invariant over the solar cycle. Data analysis of images from the STEREO Heliospheric Imager (HI) has successfully demonstrated that subtraction of the bright zodiacal light background is possible. Figure 10 shows a pair of HI images before (left panel) and after (right panel) subtraction of the zodiacal light background. The zodiacal light dominates the signal observed in the right third of the raw image. Following subtraction of the zodiacal light, a substantial amount of structure in the underlying scene is revealed.

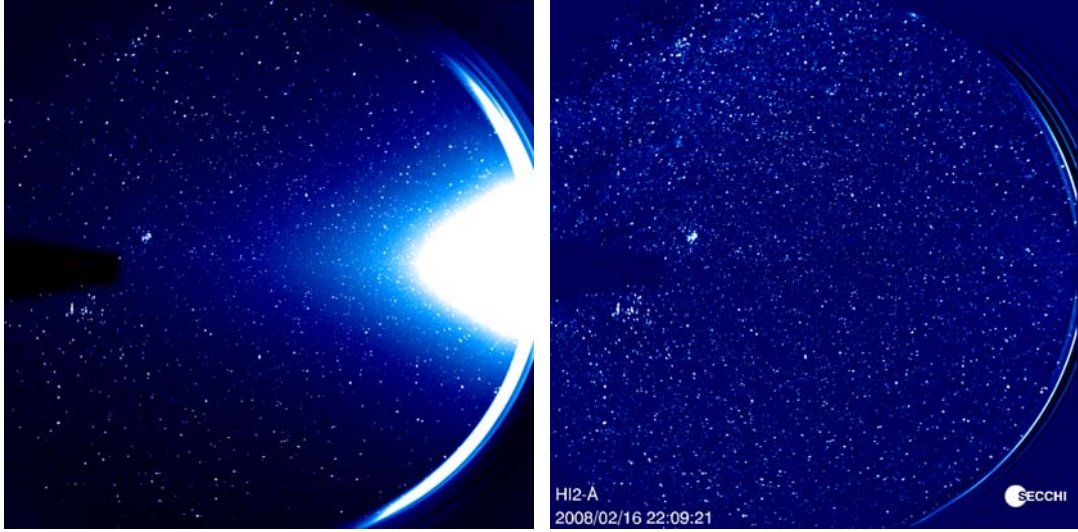


Fig. 10 – Images from the STEREO Heliospheric Imager before (left) and after (right) subtraction of the zodiacal light. Note that the structure in the right panel is mostly due to stars and not noise.

3.3.2 Instrumental Scattered Light

Another significant contribution to the scene background is the light that diffracts around the occulter of the telescope making the Thomson scattering observation. The intensity of the stray light from the occulter will be some small fraction of the full-disk brightness of the Earth. The brightness of the Earth's disk is computed as the mean solar flux ($F = 2.14 \times 10^{17}$ photons $\text{cm}^{-2} \text{ s}^{-1} \text{ sr}^{-1}$) multiplied by the Earth's albedo, ~ 0.37 . The curves shown in Fig. 11 are the fraction of the full terrestrial disk brightness that is scattered around representative internal (solid line) and external (dashed line) occulters as a function of radial distance away from the disk of the Earth. These curves are based on the stray light rejection performance data from the C2 and C3 coronagraphs of the SOHO LASCO instrument.

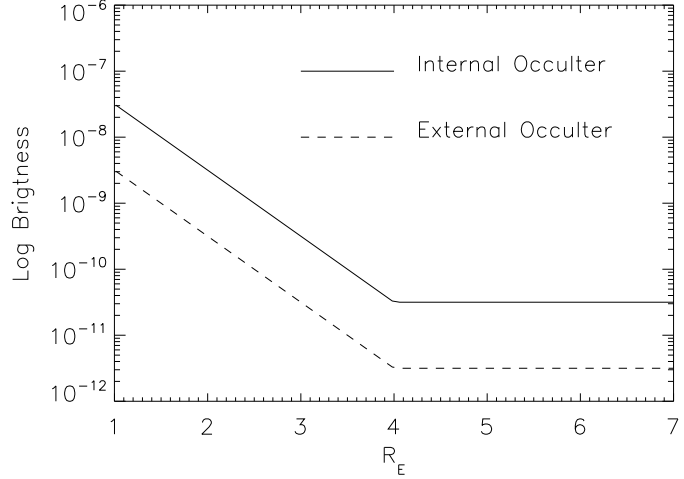


Fig. 11 – Representative scattered light curves for internal (solid) and external (dashed) occulters. The brightness here is the fraction of the occulted object’s brightness that is scattered around the occulter shown as a function of radial distance away from the object – in this case, the occulted Earth.

For a viewing location at L1, the scattered light contribution to the scene is modeled for an external occulter using the bottom curve in Fig. 11 and shown in units of Rayleighs in Fig. 12. At close radial distances to the Earth, the scattered light contribution to the scene brightness is about 150 Rayleighs, about an order of magnitude less than the zodiacal light but still about a factor of three or four brighter than the Thomson scattering signal from electrons near the ionosphere-plasmasphere boundary. At larger radial distances, the instrumental scattered light contribution falls off to less than 20 Rayleighs. For the polar viewing scenario, the scattered light brightness is taken to be the same as that shown in Fig. 12 for the sunlit side of the Earth. Assuming sufficient stray light characterization is performed during an instrumental calibration, removal of this background source is straightforward.

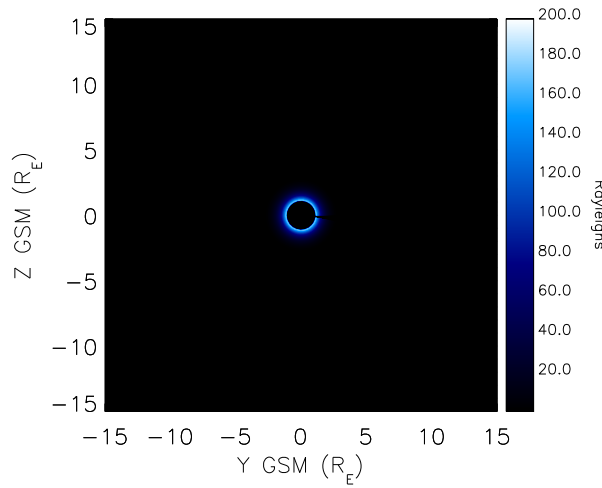


Fig. 12 – Modeled scattered light contribution to the scene as observed from L1

3.3.3 Hydrogen Geocorona Line Emissions

Another possible source of background noise in the observed scene is the emission lines in the visible part of the spectrum from the hydrogen geocorona. The upper-most portion of the Earth's neutral atmosphere (the exosphere), extending out to tens of thousands of kilometers in altitude, consists mainly of atomic hydrogen. These hydrogen atoms mainly scatter solar far-ultraviolet (FUV) photons, but emission lines also exist in the visible that fall near or within our expected band pass. These are the Balmer series H- α (656.3 nm) and H- β (486.1 nm) lines. We have chosen the short wavelength cutoff of our band pass (490 to 870 nm) to exclude the H- β line. On the other hand, H- α falls within our band pass, and it will be necessary to filter out this emission line. Emission lines from He $^+$ also exist within this general spectral region (i.e., He $^+$ 30.4 nm emission used by the IMAGE EUV experiment to image the plasmasphere), but these occur at much shorter wavelengths.

We conclude that the hydrogen emission lines do not prevent the observation of the Thomson scattering signal in the regions of interest in geospace. Band pass selection and filtering are sufficient to omit the hydrogen emission lines from the observed scene.

3.3.4 Solar Wind Contribution

Because the Thomson scattering signal is very optically thin, there will be contributions to the scene from solar wind electrons beyond the boundaries of the magnetosphere. For the purposes of remote sensing magnetospheric, plasmaspheric, and ionospheric electron densities, the Thomson scattering signal from electrons outside geospace are considered background. For example, in our Thomson scattering signal calculations from the L1 viewing location, the modeled electron densities in the magnetotail stop at about 300 R_E behind the Earth. However, since we are viewing within the ecliptic plane, we expect a non-trivial contribution from the solar wind electrons that lie beyond 300 R_E that fall within the lines of sight.

We estimate the Thomson scattering contribution from these solar wind electrons for an observing location at L1 to assess the magnitude of this effect. We assume that at radial distances beyond 300 R_E behind the Earth, the electron densities are uniform. We compute the average electron column density (TEC) in the last two-dimensional Y-Z slice of the LFM electron density model with thickness $dx = 1$ R_E located at X_{GSM} = -300 R_E and assume this value for all lines of sight. For distances beyond 300 R_E, we allow the average electron density and the solar flux to fall off as r^{-2} for segments that are each 1 R_E thick. We found that electrons at distances out to \sim 5 AU contributed as a secondary Thomson scattering source. During periods of quiescent solar wind and magnetospheric activity, this secondary Thomson scattering source contributes about 10 Rayleighs to the scene brightness. During storm periods, this secondary source can contribute up to 50 Rayleighs. Thus, for this geometry, this contribution is small compared to the zodiacal light.

4. ORBITS

This section summarizes the result of a trade study that was performed to determine suitable orbits for a mission to image geospace using Thomson scattering. In general, we considered five orbit types:

1. First Sun-Earth Lagrangian point (L1)
2. Circular equatorial Earth orbit with an altitude between about 30 and 50 R_E, which has many similarities with the lunar orbit at \sim 57 R_E
3. Elliptical, precessing Earth orbit at about 30 R_E

4. Circular, polar Earth orbit with a constant beta angle of $\sim 90^\circ$ at about $30 R_E$
5. Inertial, polar Earth orbit at about $30R_E$

The following discusses several pros and cons for each of those orbits, which are also summarized by color codes in Fig. 13.

Local Time Coverage: Complete local time coverage in “single” exposures can be achieved from locations above the pole, where all longitudes are visible simultaneously. Both orbits 4 and 5 provide this location for part of the time. Orbit 2 and 3 lack the ability to see all longitudes in one scene, but they do provide measurements of different local times throughout the mission. Orbit 1 always views toward the noon location and thus sees the dusk and dawn side on the Earth’s limb without any significant variation throughout the mission.

Background Signal: The background signal is dominated by the zodiacal light, which maximizes for lines of sight within the ecliptic and low ($\sim 0^\circ$) and high ($\sim 180^\circ$) values for ecliptic longitude. The smallest zodiacal light contribution is expected for a polar view point. Note, however, that for a polar perspective, the scattering angle for the Thomson signal is about 90° , which also decreases the Thomson signal.

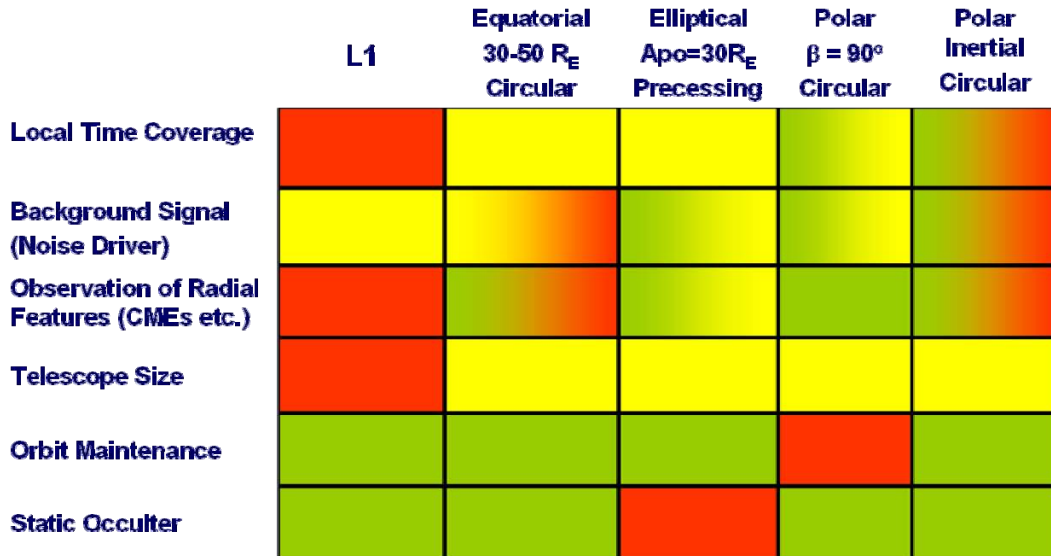


Fig. 13 – Orbit tradeoff matrix. Red stands for a clear disadvantage or technical difficulty, green for an advantage or technical feasibility, and yellow for an intermediate situation. Two colors are used for cases in which the quality of a criterion varies significantly during each orbit or during different times of the year.

Observation of Radial Features: The observation of radial features, for example CMEs that can be approximated crudely as plane wave fronts propagating toward Earth, is best achieved with fields of view that are perpendicular to the Earth-Sun line. Thus, orbits 2 through 5 are favored over orbit 1, which always views parallel to the Earth-Sun line with very limited capability to capture the temporal development of the radial features.

Telescope Size: The main driver for determining telescope size is the desired signal-to-noise ratio and, thus, mainly the background signal brightness and the distance to the observer. Since the zodiacal light increases for fields of view within the ecliptic plane and high ($\sim 180^\circ$) and low ($\sim 0^\circ$) ecliptic longitude (see Fig. 7), fields of view perpendicular to the ecliptic plane are favored. Note, however, that a scattering angle of $\sim 90^\circ$ also minimizes the Thomson scattering signal (see Section 3.1). Moreover, the feasibility of large area detectors feeds into this trade. We find that current technology is able to support the telescopes baselined for a $30 R_E$ orbit. Considering the above, we find that an orbit altitude of $\sim 30 R_E$ is a good compromise between signal strength, angular field of view of the instruments, and technical feasibility of detectors. Therefore, we favor this altitude over the lunar orbit ($\sim 57 R_E$) or L1 (235 R_E).

Orbit Maintenance: Station-keeping is only required for orbit 4 to maintain the beta angle. An assessment of the required amount of propellant to maintain this type of orbit resulted in a major concern about total mass, so that we did not further consider this orbit option in this study. The use of solar sails to perform station-keeping has been considered but their application for this mission concept has not been examined in detail and will require further study.

Static Occulter: A static occulter can be used for all observations that maintain the same distance from Earth. Only orbit 3, the elliptical orbit, would require a changing occulter to be able to make measurements throughout the entire orbit. However, a static occulter designed for the apogee distance would provide optimal measurements for part of the orbit, thus providing a viable option for a demonstration mission.

In summary we propose a polar, circular, inertial Earth orbit ($\sim 30 R_E$) for this mission. The required launch vehicle capability for this type of orbit mandates an EELV such as an Atlas V. We further find that an elliptical Earth orbit (apogee $\sim 30 R_E$) is a suitable lower-cost option for a demonstration mission.

5. SIMULATED OBSERVATIONS

We present simulated observations of the Thomson scattering signal from electrons in the near-Earth space environment. We focus on simulating the Thomson scattering measurements from a polar viewing perspective based on our analysis in Section 4. Figure 14 shows a simulated Thomson scattering observation from a telescope with an occulter blocking out the disk of the Earth to a radius of $1.185 R_E$ (center square) and two side-looking, unocculted telescopes (left and right squares). In these simulated images, we have assumed an input aperture diameter of 23.5 cm and a pixel plate scale of 270 km. The integration time for the frames shown in Figs. 14 and 15 is assumed to be 7.5 minutes, which is the time step of the LFM and SAMI model outputs. We add Gaussian distributed shot noise and assume 50% vignetting across the inner and outer fields of view. For these simulations, we have omitted contributions from stars and emission lines from the hydrogen geocorona.

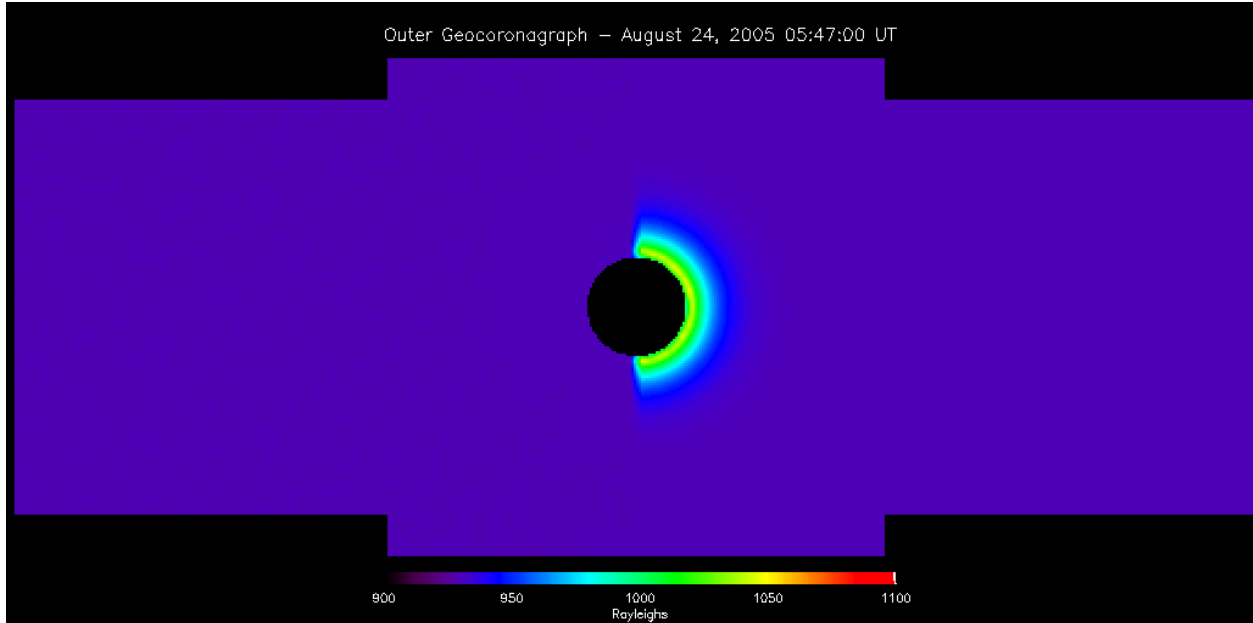


Fig. 14 – Simulated image from a polar viewing location, including Thomson scattering signal, background sources, and shot noise. The Sun is to the right and the solar wind flows from right to left. Brightnesses are scaled in units of Rayleighs. The scene is dominated by zodiacal light and, close to Earth, the instrumental background that originates from the half-illuminated Earth. The Thomson scattering from the geospace electrons is not immediately recognizable using this dynamic range and color scale.

The simulated Thomson scattering observation shown in Fig. 14 demonstrates that these measurements will be background dominated. In this image, the zodiacal light dominates the scene brightness. The instrumental scattered light contributes another 20 to 150 Rayleighs to the inner field of view of the scene on the sunlit side of the Earth.

Detailed instrument characterization and proper background subtraction will be critical for isolating the Thomson scattering signal from geospace electrons. One method of background subtraction that we have employed with reasonable success is taking the dimmest frame from a time series of images and subtracting that from the rest. Background subtracted images using this technique are shown in Figs. 15(a through f). These images have also been smoothed using a running boxcar average corresponding to $0.21 R_E \times 0.21 R_E$ in the field of view. The shot noise present in these simulated images is more apparent in these background subtracted images. Each frame shown here corresponds to the same set of Thomson scattering images shown in Fig. 6. Following background subtraction, the characteristic features of the magnetosphere, plasmasphere, and ionosphere are revealed in the images. The bow shock, magnetosheath, and magnetopause are evident near the right edge of the center image and the left edge of the right image. The structure and evolution of the plasmasphere and upper portions of the ionosphere can be discerned from these images.

Figure 15 (a through f) shows simulated observations from a Thomson scattering imager. The zodiacal light and instrumental scattered light background contributions have been subtracted by taking the dimmest image in the time series and subtracting that frame from the other images. The Sun is to the right and the solar wind flows from right to left in these images. Brightnesses are scaled in units of Rayleighs.

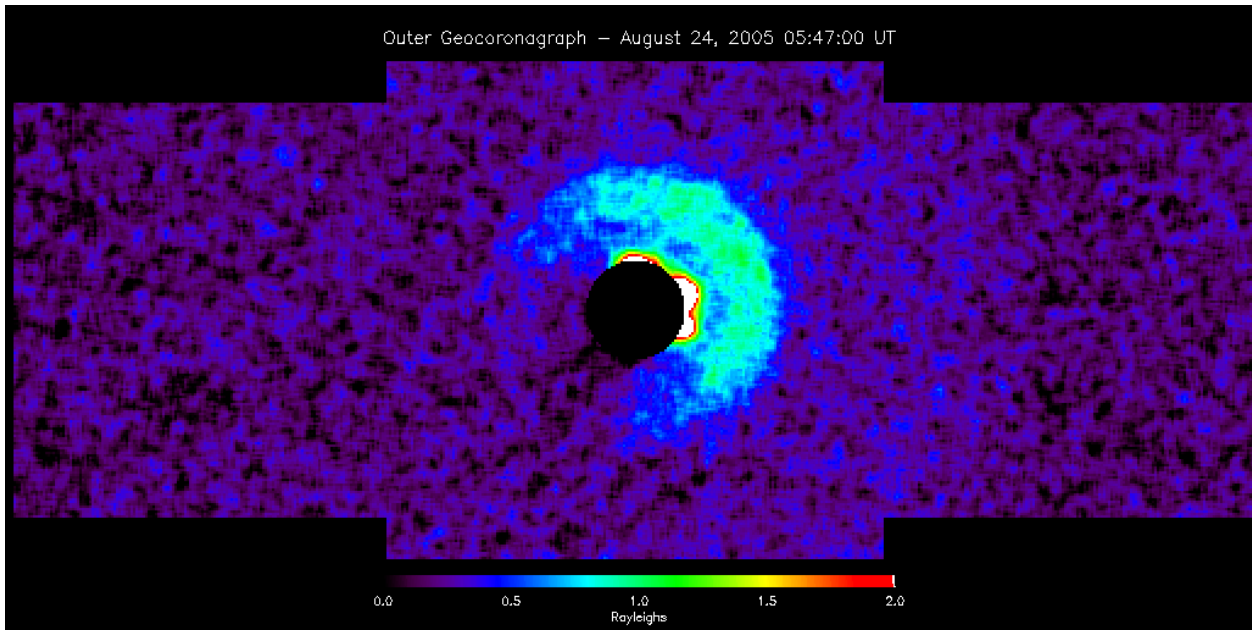


Fig. 15 (a) – Simulated observations from a Thomson scattering imager at 05:47:00 UT (background subtracted; see text)

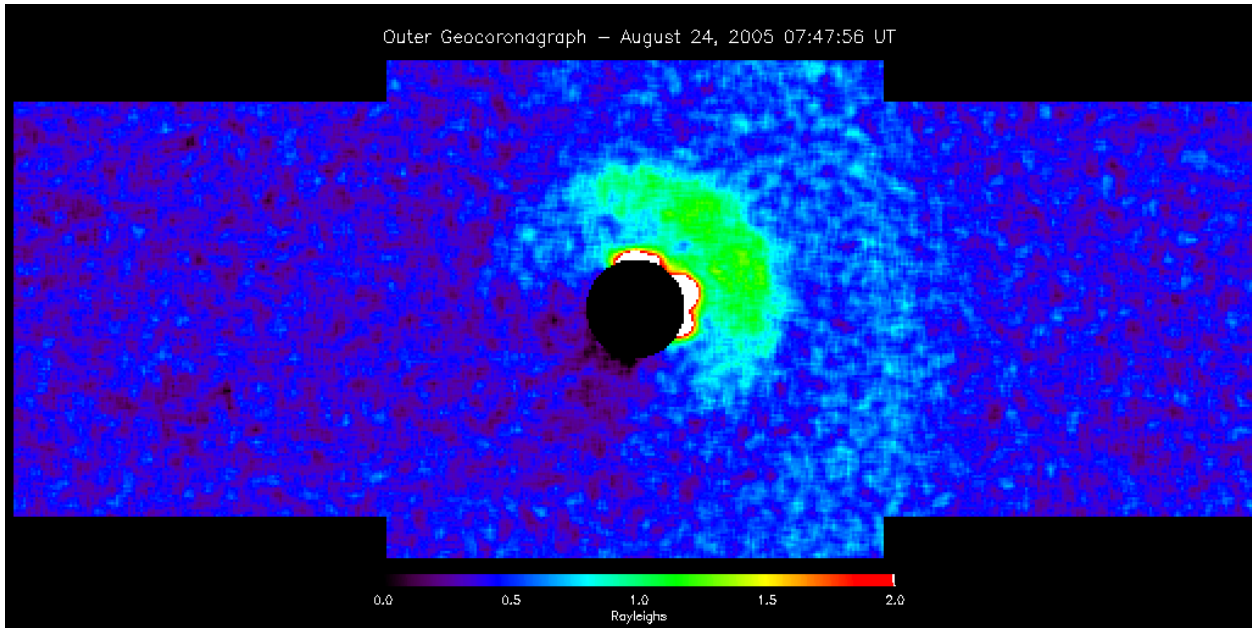


Fig. 15 (b) – Simulated observations from a Thomson scattering imager at 07:47:56 UT (background subtracted; see text)

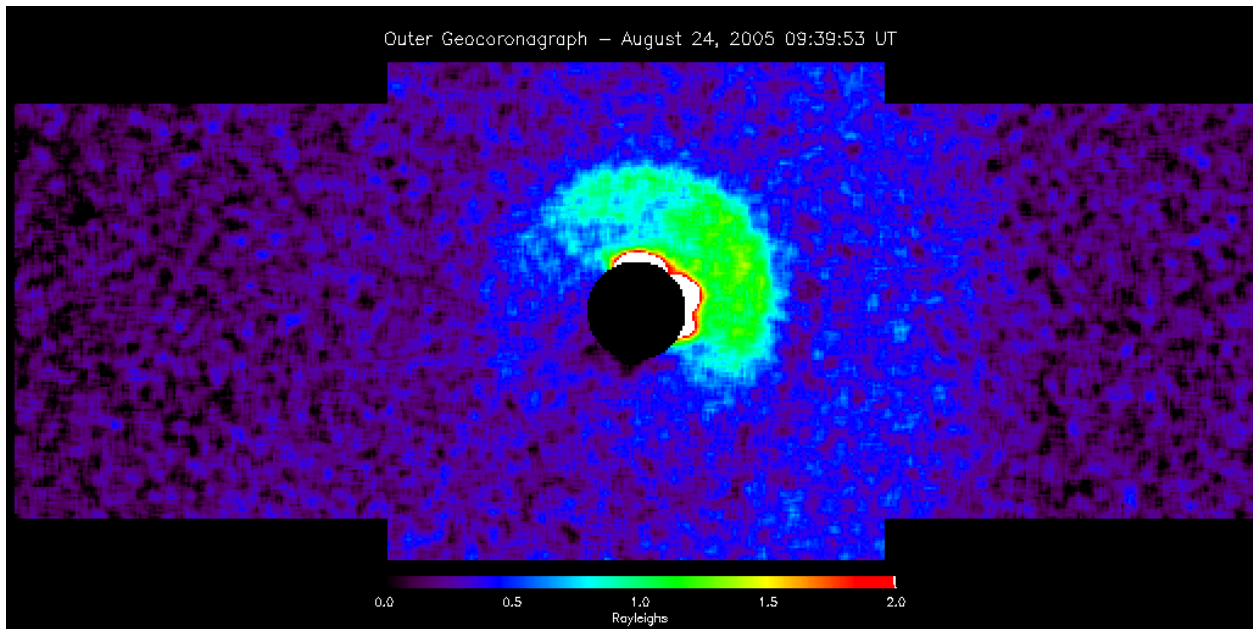


Fig. 15 (c) – Simulated observations from a Thomson scattering imager at 09:39:53 UT (background subtracted; see text)

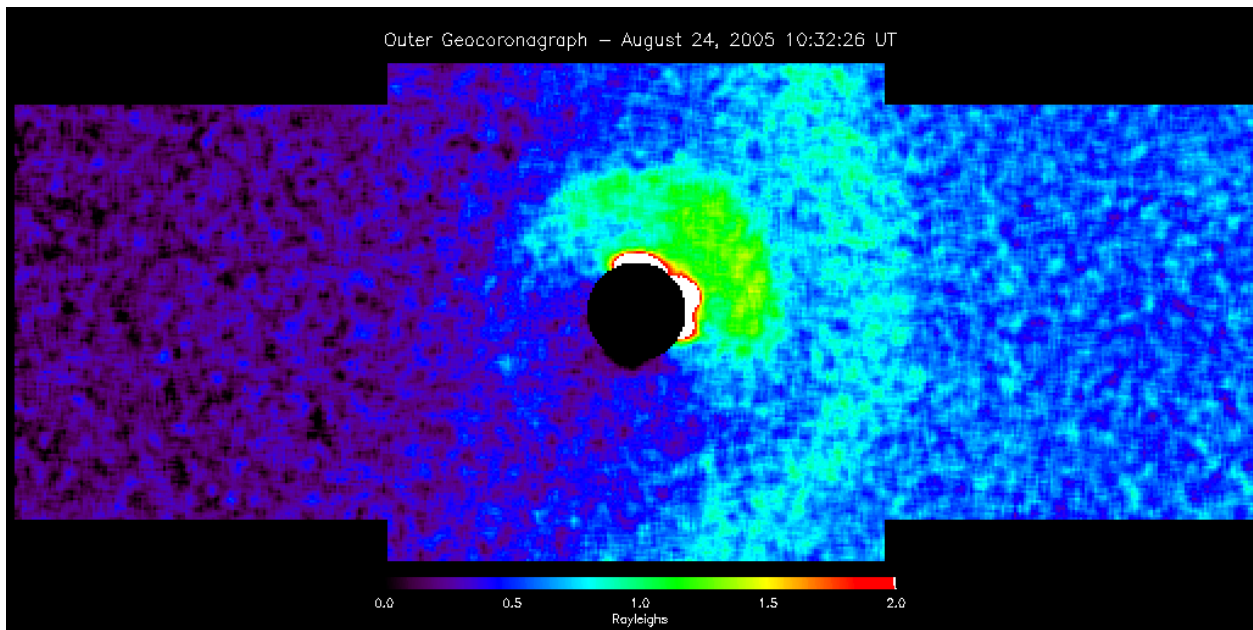


Fig. 15 (d) – Simulated observations from a Thomson scattering imager at 10:32:26 UT (background subtracted; see text)

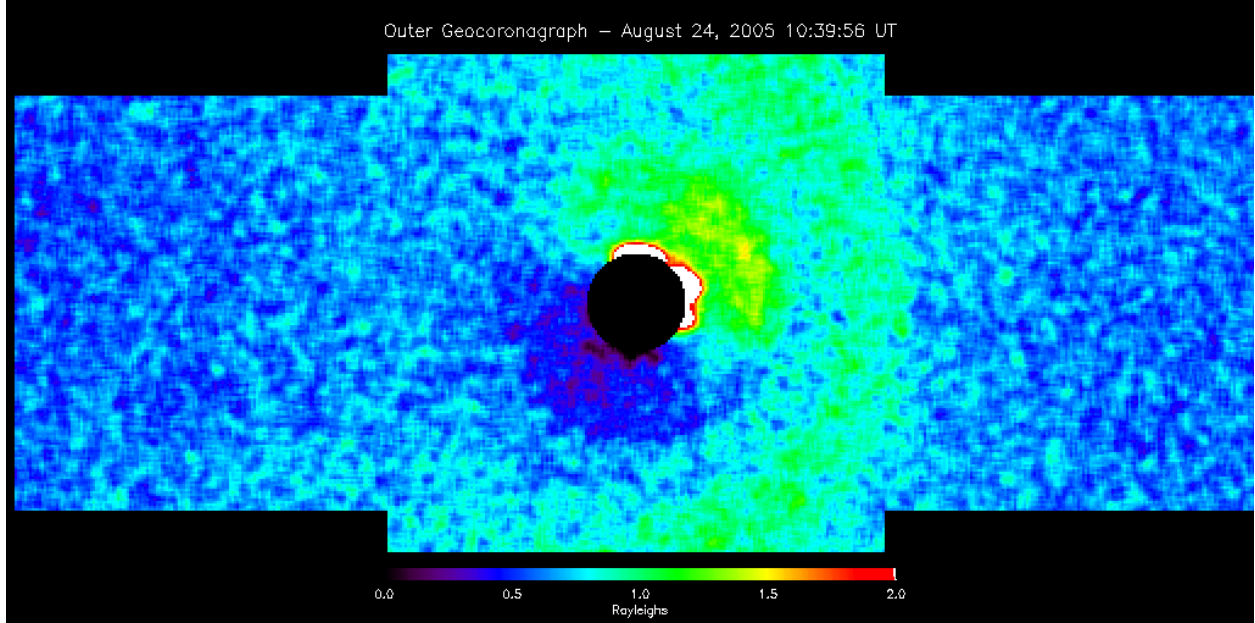


Fig. 15 (e) – Simulated observations from a Thomson scattering imager at 10:39:56 UT (background subtracted; see text)

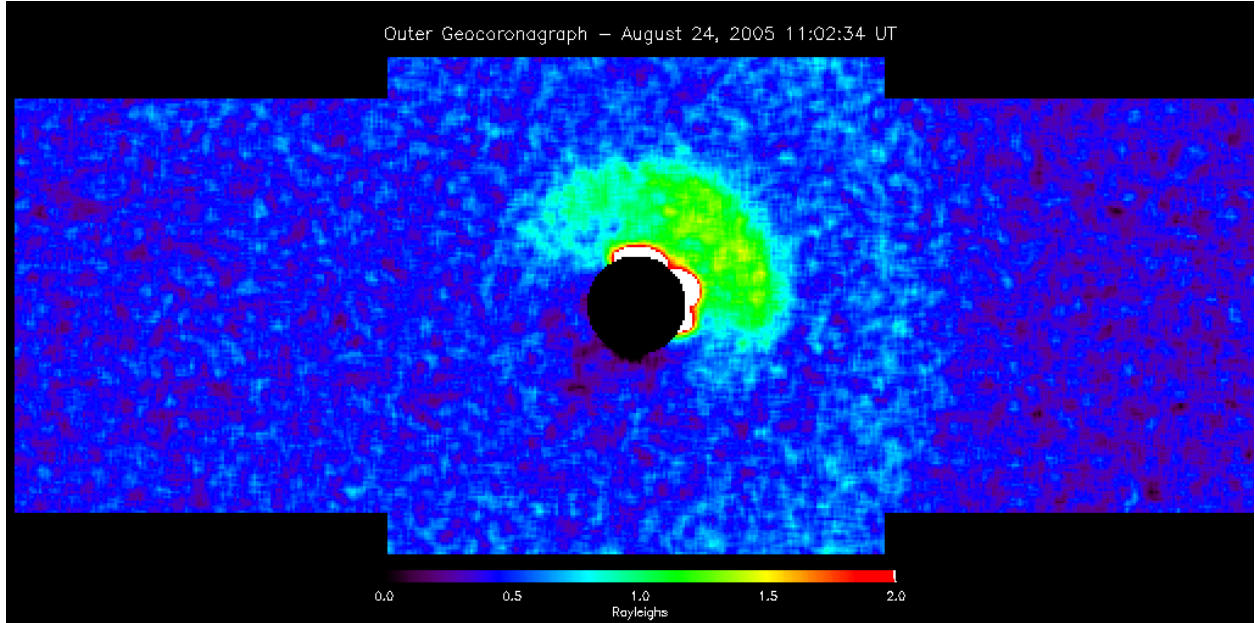


Fig. 15 (f) – Simulated observations from a Thomson scattering imager at 11:02:34 UT (background subtracted; see text)

We also explored the capabilities of a Thomson scattering imager that focused on the ionosphere and plasmasphere with greater spatial resolution. Simulated observations from an Earth-centered imager with an occulter of radius $1.05 R_E$ are shown in Fig. 16. We have subtracted the background with the same technique used in Fig. 15. Shot noise is also included here. Here, we assume an input aperture diameter of 23.8 cm and a pixel plate scale of 120 km. The inner field of view begins near 320 km in altitude, which

allows us to observe the F-region of the ionosphere. The images shown in Fig. 16 demonstrate how structures in the upper F-region of the ionosphere with scale sizes of a few hundred kilometers can be observed with this imaging technique. Such observations will also allow us to provide specifications of the boundary between the ionosphere and plasmasphere.

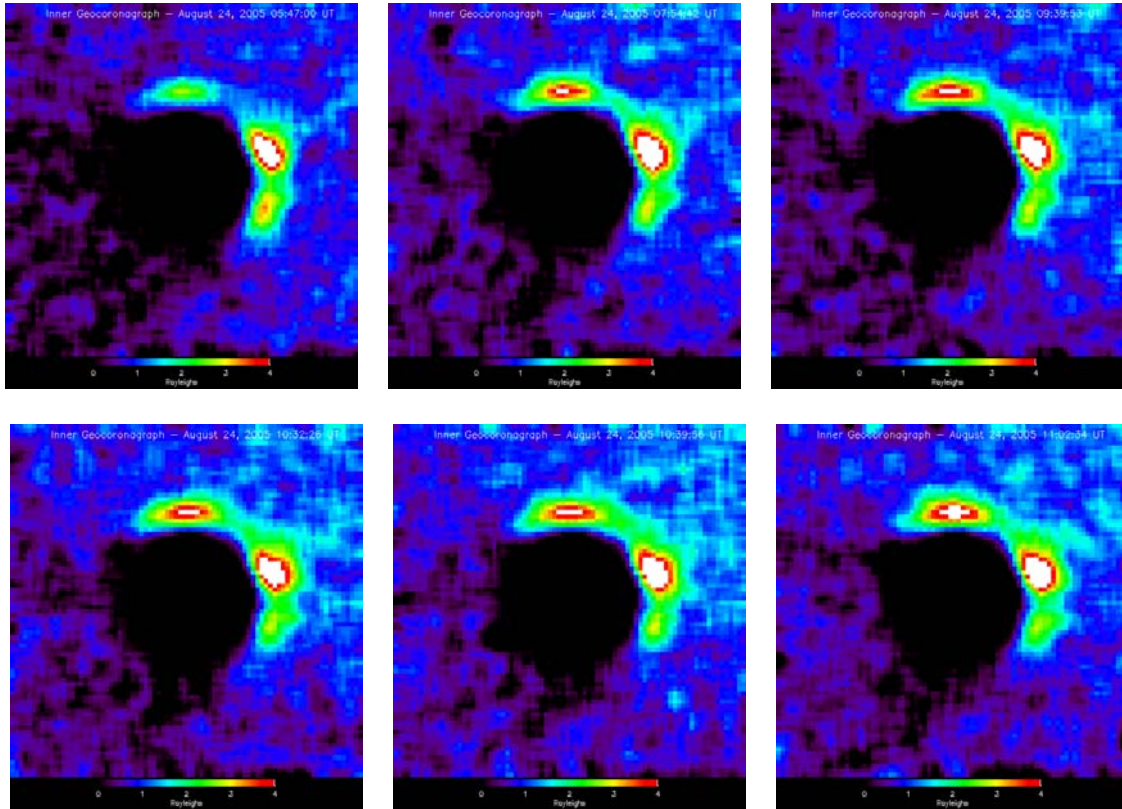


Fig. 16 – Simulated Thomson scattering observations from a polar viewing location focusing on observing the ionosphere and plasmasphere

6. PATH TO OPERATION

Transferring an innovative and not-yet-demonstrated measurement concept to an operational program usually requires several steps. The first one is the assessment of the concept feasibility, which we have accomplished with this study. The next step is to demonstrate the measurement technique on orbit, which elevates the technical readiness level (TRL) of all or a subset of the instruments to the highest level of 9. A demonstration mission will also allow the development and test of the required data analysis algorithms as well as the detailed assessment of the achievable data quality. Based on the results of the demonstration mission and a detailed set of measurement requirements that are derived from the operational needs, an operational mission can be designed and eventually realized.

The two national institutions that are most likely to ultimately use the data in their day-to-day operations are the Air Force Weather Agency (AFWA) and, on the civilian side, the NOAA Space Weather

Prediction Center (SWPC). Global images of the electron distributions in the near-Earth space environment will enable these agencies to achieve a much higher level of situational awareness in space than is now possible with existing measurements. Moreover, these Thomson scattering images of geospace will allow for the evolution of now nascent space weather models used by AFWA and NOAA SWPC into predictive tools for operational use.

REFERENCES

- Burch, J.L., 2003. "The First Two Years of IMAGE," *Space Sci. Rev.* **109**, 1-24.
- Burch, J.L., 2005. "Magnetospheric Imaging: Promise to Reality," *Rev. Geophys.* **43**, RG3001.
- Craven, P.D., D.L. Gallagher, and R.H. Comfort, 1997. "Relative Concentration of He⁺ in the Inner Magnetosphere as Observed by the DE 1 Retarding Ion Mass Spectrometer," *J. Geophys. Res.* **102**, 2279-2289.
- Fedder, J.A. and J.G. Lyon, 1995. "The Earth's Magnetosphere is 165 R_E Long: Self-Consistent Currents, Convection, Magnetospheric Structure, and Processes for Northward Interplanetary Magnetic Field," *J. Geophys. Res.- Space Physics* **100**(A3), 3623-3635.
- Fedder, J.A., J.G. Lyon, S.P. Slinker, and C.M. Mobarry, 1995a. "Topological Structure of the Magnetotail as a Function of Interplanetary Magnetic Field Direction," *J. Geophys. Res.* **100**, 3613.
- Fedder, J.A., S.P. Slinker, J.G. Lyon, and R.D. Elphinstone, 1995b. "Global Numerical Simulation of the Growth Phase and Expansion Onset of a Substorm Observed by VIKING," *J. Geophys. Res.* **100**, 19083.
- Fedder, J.A., S.P. Slinker, J.G. Lyon, C.T. Russell, F.R. Fenrich, and J.G. Luhmann, 1997. "A First Comparison of POLAR Magnetic Field Measurements and Magnetohydrodynamic Simulation Results for Field-Aligned Currents," *Geophys. Res. Lett.* **24**, 2491.
- Foster, J., P.J. Erickson, A.J. Coster, J. Goldstein, and F.J. Rich, 2002. "Ionospheric Signatures of Plasmaspheric Tails," *Geophys. Res. Lett.* **29**, doi: 10.1029/2002GL015067.
- Goldstein, J., B.R. Sandel, W.T. Forrester, and P.H. Reiff, 2003. "IMF-driven Plasmasphere Erosion of 10 July 2000," *Geophys. Res. Lett.* **30**, 1146, doi:10.1029/2002GL016478.
- Harder, J., G. Lawrence, G. Rottman, and T. Woods, 2000. "The Spectral Irradiance Monitor (SIM) for the SORCE Mission," *Proc. SPIE* **4135**, 204-214.
- Hedin, A.E., 1987. "MSIS-86 Thermospheric Model," *J. Geophys. Res.* **92**, 4649.
- Hedin, A.E., M.A. Biondi, R.G. Burnside, G. Hernandez, R.M. Johnson, T.L. Killeen, C. Mazaudier, J.W. Meriwether, J.E. Salah, R.J. Sica, R.W. Smith, N.W. Spencer, V.B. Wickwar, and T.S. Virdi, 1991. "Revised Global Model of the Thermosphere Winds Using Satellite and Ground-based Observations," *J. Geophys. Res.* **96**, 7657.

- Huba, J.D., G. Joyce, and J.A. Fedder, 2000. "SAMI2 (Sami2 is Another Model of the Ionosphere): A New Low-Latitude Ionosphere Model," *J. Geophys. Res.* **105**, 23,035.
- Huba, J.D., G. Joyce, S. Sazykin, R. Wolf, and R. Spiro, 2005. "Simulation Study of Penetration Electric Fields in the Low- To Mid-Latitude Ionosphere," *Geophys. Res. Lett.* **32**, L23101, doi:10.1029/2005GL024162.
- Koutchmy, S. and P.L. Lamy, 1985. "The F-Corona and the Circumsolar Dust: Evidences and Properties," in *Properties and Interactions of Interplanetary Dust*, eds. R.H. Giese and P.L. Lamy (Dordrecht, D. Reidel Publishing Co.).
- Krall, J., J.D. Huba, and J.A. Fedder, 2008. "Simulation of Field-aligned H⁺ and He⁺ Dynamics During Late-stage Plasmasphere Refilling," *Ann. Geophys.* **26**, 1507-1516.
- Kwon, S.M., S.S. Hong, and J.L. Weinberg, 2004. "An Observational Model of the Zodiacal Light Brightness Distribution," *New Astron.* **10**, 91-107.
- Leinert, Ch., S. Bowyer, L.K. Haikala, M.S. Hanner, M.G. Hauser, A.-Ch. Levasseur-Regourd, I. Mann, K. Matilla, W.T. Reach, W. Schlosser, H.J. Staude, G.N. Toller, J.L. Weiland, J.L. Weinberg, and A.N. Witt, 1998. "The 1997 Reference of Diffuse Sky Brightness," *Astron. Astro-phys. Suppl. Ser.* **127**, 1-99.
- Lyon, J.G., J.A. Fedder, and C.M. Mobarry, 2004. "The Lyon-Fedder-Mobarry (LFM) Global MHD Magnetospheric Simulation Code," *J. Atmos. Sol. Terres. Phys.* **66**, 1333.
- Meier, R.R., 1991. "Ultraviolet Spectroscopy and Remote Sensing of the Upper Atmosphere," *Space Science Rev.* **58**, 1.
- Meier, R.R., 2007a. "A Technique for Imaging Electrons in the Near-Earth Space Environment," US Patent Pending, Navy Case No. 98,826.
- Meier, R.R., 2007b. "Geospace Imaging: The Big Picture," American Geophysical Union Fall Meeting, SA24B, San Francisco.
- Mobarry, C.M., J.A. Fedder, and J.G. Lyon, 1996. "Equatorial Plasma Convection from Global Simulations of the Earth's Magnetosphere," *J. Geophys. Res.* **101**, 7859.
- Picone, J.M., A.E. Hedin, D.P. Drob, and A.C. Aikin, 2002. "NRLMSISE-00 Empirical Model of the Atmosphere: Statistical Comparisons and Scientific Issues," *J. Geophys. Res.* **107**, doi: 10.1029/2002JA009430.
- Robinson, R.M., R.R. Vondrak, K. Miller, T. Dabbs, and D. Hardy, 1987. "On Calculating Ionospheric Conductances from the Flux and Energy of Precipitating Electrons," *J. Geophys. Res.* **92**, 2565-2569.
- Qiu, J., P.R. Goode, E. Palle, V. Yurchyshyn, J. Hickey, P. Montanes-Rodriguez, M.-C. Chu, E. Kolbe, C.T. Brown, and S.E. Koonin, 2003. "Earthshine and the Earth's Albedo: 1. Earthshine Observations and Measurements of the Lunar Phase Function for Accurate Measurements of the Earth's Bond Albedo," *J. Geophys. Res.* **108**(D22), 4709, doi:10.1029/2003JD003610.

- Slinker, S.P., J.A. Fedder, J. Chen, and J.G. Lyon, 1998. "Global MHD Simulation of the Magnetosphere and Ionosphere for 1930-2330 UT on November 3, 1993," *J. Geophys. Res.* **103**, 26,243.
- Slinker, S.P., J.A. Fedder, W.J. Hughes, and J.G. Lyon, 1999a. "Response of the Ionosphere to a Density Pulse in the Solar Wind: Simulation of Traveling Convection Vortices," *Geophys. Res. Lett.* **26**, 3549.
- Slinker, S.P., J.A. Fedder, B.A. Emery, K.B. Baker, D. Lummerzheim, J.G. Lyon, and F.J. Rich, 1999b. "Comparison of Global MHD Simulations with AMIE Simulations for the Events of May 19-20, 1996," *J. Geophys. Res.* **104**, 28379.
- Vourlidas, A. and R.A. Howard, 2006. "The Proper Treatment of Coronal Mass Ejection Brightness: A New Methodology and Implications for Observations," *Astrophys. J.* **642**, 1216.